 doi:10.20944/preprints202011.0704.v1

Article

Light Management in Single Rectangular Silicon Nanowires for Photovoltaic Applications

Wenfu Liu [1,*]

[1] School of Mechanical and Energy Engineering, Huanghuai University, Zhumadian, Henan 463000, China
* Correspondence: liuwenfu@huanghuai.edu.cn (W.L.)

Abstract: Light management in single nanowires (NWs) is of great importance for photovoltaic applications. However, square NWs (SNWs) can limit their light-trapping ability due to high geometrical symmetry. In this work, we present a detailed study of light management in single silicon NWs with a rectangular cross-section (RNWs). We demonstrate that the RNWs exhibit significantly enhanced light-harvesting compared with the SNWs, which can be attributed to the symmetry-broken structure that can orthogonalize the direction of light illumination and the leaky mode resonances (LMRs). That is, the rectangular cross-section can simultaneously increase the light path length by increasing the vertical side and reshape the LMR modes by decreasing the horizontal side. We found that the light absorption can be engineered via tuning the horizontal and vertical sides, the photocurrent is significantly enhanced by 276.5% or 82.9% in comparison with that of the SNWs with the same side length as the horizontal side of 100 nm or the vertical side of 1000 nm, respectively. This work advances our understanding of how to improve light-harvesting based on the symmetry breaking from the SNWs to RNWs and provides an effective way for designing high-efficiency single NW photovoltaic devices.

Keywords: silicon; single nanowires; rectangular cross-section; absorption; photocurrent

1. Introduction

Single nanowire (NW) solar cells have increasingly attracted attention in recent years serving as powering nanoscale devices [1-8]. Light management in single NW solar cells is very important for ensuring both high absorption and little material [9-14]. Therefore, light management is an effective way to improve light absorption and enhance the photoelectric conversion efficiency of single NW solar cell. It is well known that the strong interaction between the incident light and a single NW has been applied to dramatically increase light trapping due to the leaky mode resonances (LMRs) [15-17]. However, the overall light-trapping performance of a single NW is still far below expectations owing to the narrow resonant peaks.

Therefore, a great variety of strategies have been employed to improve light-harvesting ability. It has been shown that the light absorption could be readily engineered by controlling the size, geometry and orientation of the NWs [18-24]. Our previous studies [25-27] showed that the light absorption could be further improved by introducing a non-absorbing dielectric shell (or graded dual shells) as the antireflection coating, which was experimentally and numerically demonstrated in the recent studies [28-32]. Recently, some new strategies have been implemented to improve the light-harvesting capability of the NWs based on the symmetry breaking. For example, front (or rear)-opening crescent design [33,34], off-axial core-shell design [35,36], asymmetrical nanovoid design [20], partially capped design [37-40], nanocone design [41-44], inclined design [45-47], disorder design [48-52] and crescent nanohole design [53]. More recently, we investigated the symmetry structure from circular NWs to elliptical NWs [54]. Similarly, compared with the square NWs (SNWs), rectangular NWs (RNWs) provide more possibility to realize effective light management. It is worth noting that the square or rectangular nanostructures have been applied to light management [55-57]. However, to the best of our knowledge, very few investigations based on the symmetry

Preprints (www.preprints.org) | NOT PEER-REVIEWED | Posted: 27 November 2020 doi:10.20944/preprints202011.0704.v1

breaking from the SNWs to RNWs have been explored to improve light-harvesting in single NWs so far.

In this work, we carry out detailed investigations on the light-trapping effect of single RNWs. We demonstrate that the giant enhancement of the light absorption occurs when the RNWs replace the SNWs. The detailed analysis of the electric field, absorption mode profile and photogeneration rate shows that this enhancement is mainly attributed to the asymmetry breaking from the SNWs to RNWs. Specifically, the light path length can be increased by increasing the vertical side and the LMR modes can be reshaped by decreasing the horizontal side. Simulation results reveal that the photocurrent is significantly enhanced by 276.5% or 82.9% compared with that of the SNWs with the same side length as the horizontal side of 100 nm or the vertical side of 1000 nm, respectively.

2. Model and Methods

2.1. Model

Figure 1 schematically shows the cross-sectional views of a RNW and two SNWs. The horizontal (x) and vertical (y) axes of the RNWs are denoted by a and b. The horizontal (or vertical) side is perpendicular (or parallel) to the light illumination direction, as presented using the colorful arrows in Figure 1. Note here that the unpolarized light (e.g., sunlight) can be expressed as the average of transverse electric (TE, electric field normal to the NW axis) and transverse magnetic (TM, magnetic field normal to the NW axis) light. The values of a and b are chosen to be 300 and 100 nm as the typical representative nanoscale size, respectively. It should be noted that the SNWs are also shown for comparison, where the side lengths of the SNWs are chosen to be 300 and 100 to investigate the improved light absorption performance due to the reshaped LMRs by decreasing a and the increased light path length by increasing b. Silicon is chosen as a typical semiconductor material and its wavelength-dependent refractive index is adopted from the experimental data [58].

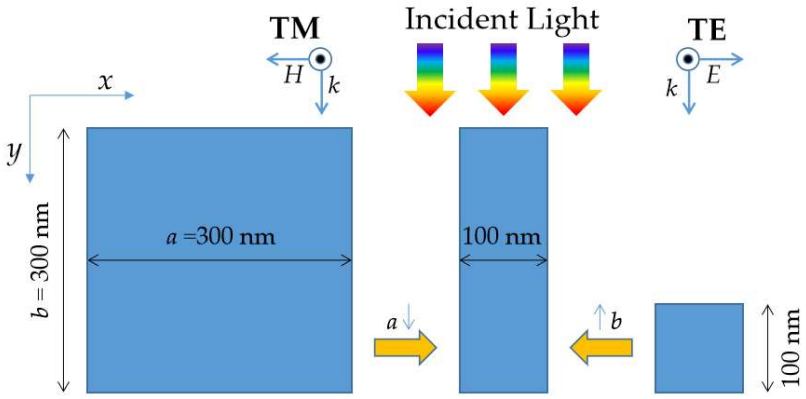

Figure 1. Schematics of the cross-section of a rectangular nanowire (RNW) and two square nanowires SNWs). The geometrical metrics used to describe the geometry of the RNW, the horizontal (x) side a and the vertical (y) side b, are presented. A representative value of a and b of the RNW are chosen to be 100 and 300 nm, respectively. The side lengths of the SNWs are chosen to be 300 or 100 nm for comparison, the material of the RNW is set to be silicon as a representative semiconductor and the light illumination is perpendicular to the axis of the RNW from above. Note that the unpolarized light (e.g., sunlight) illumination can be regarded as the average of transverse electric (TE, electric field normal to the NW axis) and transverse magnetic (TM, magnetic field normal to the NW axis) light illumination.

2.2. Methods

Numerical simulations are performed by solving Maxwell's equations based on the two-dimensional finite difference time domain (2D FDTD) method [59-61] by assuming that the length of the NW is far larger than the size of the cross-section, which can be referred to the work of Kim and

Preprints (www.preprints.org) | NOT PEER-REVIEWED | Posted: 27 November 2020 doi:10.20944/preprints202011.0704.v1

co-workers for details [22-24,30]. In this simulation, the RNW is illuminated normally by sunlight from the top, the wavelength range of the incident light is from 300 to 1100 nm with a step size of 5 nm considering solar radiation and the bandgap of silicon, the perfectly matched layers (PML) boundary conditions are considered to avoid any non-physical reflection with the boundaries, the total-field scattered-field (TFSF) method was applied to ensure that a single NW interacts with an infinite plane wave. Also, the minimum cell size of the FDTD mesh is set to from 0.05 to 5 nm corresponding to b (from 5 to 1000 nm) to guarantee the accuracy of the simulation results.

2.2.1. The Normalized Electric Field (E_r)

The normalized electric field (E_r) can be expressed as [37]:

$$E_r = E/E_0 , \tag{1}$$

where E is the electric field of the RNWs, which is obtained by FDTD numerical simulation, and E_0 is the electric field of the incident light, respectively.

2.2.2. The Absorption Mode Profile (P_{abs})

The wavelength-dependent absorption mode profile (P_{abs}) calculated from the Poynting theorem can be regarded as [32,39,44,62]:

$$P_{abs} = \frac{1}{2}\omega\varepsilon''|E|^2 , \tag{2}$$

where ω is the angular frequency of the incident light and ε'' is the imaginary part of the permittivity of silicon, respectively.

2.2.3. The Absorption Efficiency (Q_{abs})

To qualify the light absorption performance of the RNWs, we define the absorption efficiency (Q_{abs}) as [32,39,44,62]:

$$Q_{abs} = C_{abs}/C_{geo} , \tag{3}$$

where C_{geo} is the projected area per unit length of the RNWs and C_{abs} is the absorption cross-section per unit length obtained by,

$$C_{abs} = \frac{\iint P_{abs}\,dxdy}{I_0} = k_0\varepsilon_r''\iint |E_r|^2\,dxdy , \tag{4}$$

where k_0 is the wave vector in air, ε_r'' is the imaginary part of the relative permittivity of silicon, x and y are the coordinate axes shown in Figure 1, and I_0 is the solar incident light intensity expressed as [32,39,44,62]:

$$I_0 = \frac{1}{2}c\varepsilon_0|E_0|^2 , \tag{5}$$

$$\varepsilon_r'' = \varepsilon''/\varepsilon_0 , \tag{6}$$

where c is the speed of light and ε_0 is the permittivity in air, respectively.

2.2.4. The Photogeneration Rate (G)

The spatially dependent photogeneration rate (G) is readily calculated by [63,64]:

$$G = \int_{300}^{1100}\frac{P_{abs}}{\hbar\omega}d\lambda = \int_{300}^{1100}\frac{\varepsilon''|E|^2}{2\hbar}\mathrm{d}\lambda , \tag{7}$$

Preprints (www.preprints.org) | NOT PEER-REVIEWED | Posted: 27 November 2020 doi:10.20944/preprints202011.0704.v1

where $\hbar$ is the reduced Planck's constant and λ is the wavelength of the incident light. It should be impressed that when using Equation (7), each photon absorbed in the RNW contributes to the photocurrent without considering recombination losses.

2.2.5. The Ultimate Photocurrent (J_{ph})

The overall light absorption performance is evaluated using the ultimate photocurrent (J_{ph}) calculated by:

$$J_{ph} = \frac{q}{C_{geo}} \iint G dx dy = q \int_{300}^{1100} \Gamma(\lambda) Q_{abs}(\lambda) d\lambda \,, \tag{8}$$

where q is the elementary charge and Γ is the AM1.5G standard solar photon flux density spectrum. It should be noted here that 100% collection efficiency is assumed, which has been widely employed to evaluate the ultimate photocurrent [16,64].

2.2.6. The Photocurrent Enhancement Factor (PEF)

The photocurrent enhancement is evaluated by employing the photocurrent enhancement factor (PEF) using the relation:

$$\text{PEF} = \left(J_{ph,RNWs} - J_{ph,SNWs} \right) \Big/ J_{ph,SNWs} \,, \tag{9}$$

where $J_{ph,RNWs}$ and $J_{ph,SNWs}$ are the photocurrent density for the RNWs and SNWs, respectively.

3. Results and Discussion

3.1. Light absorption Mechanism in Single RNW

To understand the light absorption mechanism responsible for the improved photocurrent of the RNW, we investigate the absorption efficiency (Q_{abs}), ultimate photocurrent (J_{ph}), normalized electric field (E_r), absorption mode profile (P_{abs}) and photogeneration rate (G), respectively. Note here that a = 100, b = 300 nm and the side lengths of the SNW are chosen to 300 (SNW1) and 100 (SNW2) nm for comparison, respectively.

3.1.1. The Absorption Efficiency (Q_{abs})

To quantitatively characterize the light absorption performance of the RNW compared with the SNW, we first examine the absorption spectra calculated by Equation (3). In Figure 2, we show λ-dependent Q_{abs} spectra of the RNW with a = 100 and b = 300 nm and the RNWs with a = b = 300 and 100 nm under TM, TE and unpolarized light, respectively. Firstly, Q_{abs} of the RNW is much bigger than that of the SNW2 almost the whole wavelength range, except for 560 < λ < 615 nm near the 3rd absorption peak of the SNW2 for TM light, 430 < λ < 455 nm near the 2nd absorption peak of the SNW2 for TE light and 560 < λ < 610 nm for near the 3rd absorption peak of the SNW2 for unpolarized light, which can lead to a significant photocurrent enhancement. Secondly, Q_{abs} of the RNW is much bigger than that of the SNW1 in the short-wavelength range of $\lambda < \lambda_{cTM}$ ~ 490, $\lambda < \lambda_{cTE}$ ~ 425 or $\lambda < \lambda_c$ ~ 485 nm for TM, TE or unpolarized light, which can result in a significant photocurrent enhancement. In contrast, the light absorption of the RNW seems to be comparable in the long-wavelength range of $\lambda > \lambda_{cTM}$, $\lambda > \lambda_{cTE}$ or $\lambda > \lambda_c$, which can lead to a little contribution to the photocurrent enhancement. Note here that λ_{cTM}, λ_{cTE} and λ_c are the characteristic wavelengths for TM, TE and unpolarized light, below which the light absorption is always enhanced and can be readily determined for a fixed a and b.

Preprints (www.preprints.org) | NOT PEER-REVIEWED | Posted: 27 November 2020 doi:10.20944/preprints202011.0704.v1

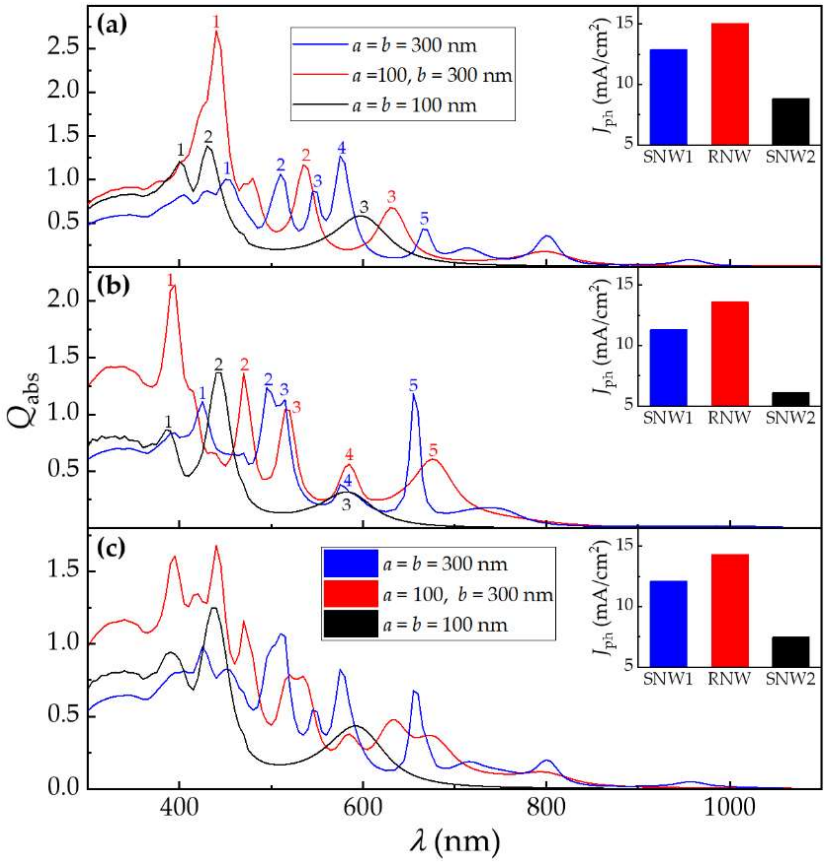

Figure 2. Absorption efficiency (Q_{abs}) of the SNW and RNW as a function of wavelength (λ) for (**a**) TM, (**b**) TE and (**c**) unpolarized light illumination, respectively. The insets at the top right corner show the ultimate photocurrent (J_{ph}) of the SNW and RNW for (**a**) TM, (**b**) TE and (**c**) unpolarized light, respectively. Note that a = 100 and b = 300 nm.

More importantly, the Q_{abs} spectra exhibit two strong absorption peaks in the wavelength range of $\lambda < \lambda_{cTM}$ or $\lambda < \lambda_{cTE}$ for TM or TE light, respectively. Specifically, the Q_{abs} value reaches 2.71 near λ = 440 nm for TM light and 2.14 near λ = 395 nm for TE light, which results in a dramatic photocurrent enhancement. Note here that some Q_{abs} values exceed unity, which is attributed to the fact that the absorption cross-section is bigger than the physical cross-section. All in all, the absorption results indicate the great potential of the single RNW in improving light-harvesting due to the symmetry-broken structure from the SNW to RNW.

3.1.2. The Ultimate Photocurrent (J_{ph})

To evaluate the light-harvesting of the RNW for photovoltaic applications, we then calculated the ultimate photocurrent (J_{ph}) according to Equation (8). For a direct comparison, in the insets of the upper right corner of Figure 2, we show J_{ph} of the RNW and SNWs corresponding to Q_{abs} for TM, TE and unpolarized light illumination, respectively. It is observed that J_{ph} of the RNW is much bigger than that of the SNW1 and SNW2. J_{ph} for TM, TE and unpolarized light illumination reaches 15.07, 13.62 and 14.35 mA/cm^2, which is 17.00%, 20.42% and 18.69% higher than that of the SNW1 (12.88, 11.31 and 12.09 mA/cm^2), respectively. It is worth noting here that the photocurrent enhancement is mainly attributed to the reshaped LMRs caused by decreasing a (here from 300 to 100 nm) compared to the SNW1, as discussed later. Moreover, J_{ph} can be dramatically enhanced due to the increased light path length by increasing b (here 100 to 300 nm) compared with the SNW2. J_{ph} is 70.5%, 121.8% and 91.6% higher than that of the SNW2 (8.84, 6.14 and 7.49 mA/cm^2) for TM, TE and unpolarized

Preprints (www.preprints.org) | NOT PEER-REVIEWED | Posted: 27 November 2020 doi:10.20944/preprints202011.0704.v1

light illumination, respectively. The photocurrent results further indicate the huge potential of light-harvesting in single RNWs for photovoltaic applications.

3.1.3. The Normalized Electric Field (E_r)

To understand the mechanism of light-harvesting in single RNWs, we first examine the normalized electric field (E_r) calculated by Equation (1). In Figure 3, we present the E_r profiles of the SNW1, RNW and SNW2 corresponding to the positions denoted by numerals in Figure 2a,b under TM and TE light illumination, respectively. Note that Figure 3a,d show the E_r profiles of the SNW1 for TM (λ = 450, 510, 545, 575 and 665 nm) and TE (λ = 425, 495, 515, 575 and 655 nm) light illumination, Figure 3b,e show those of the RNW for TM (λ = 440, 535 and 630 nm) and TE (λ = 395, 470, 515, 585 and 675 nm) light illumination, while Figure 3c,f show those of the SNW2 for TM (λ = 400, 430 and 595 nm) and TE (λ = 385, 445 and 580 nm) light illumination,respectively.

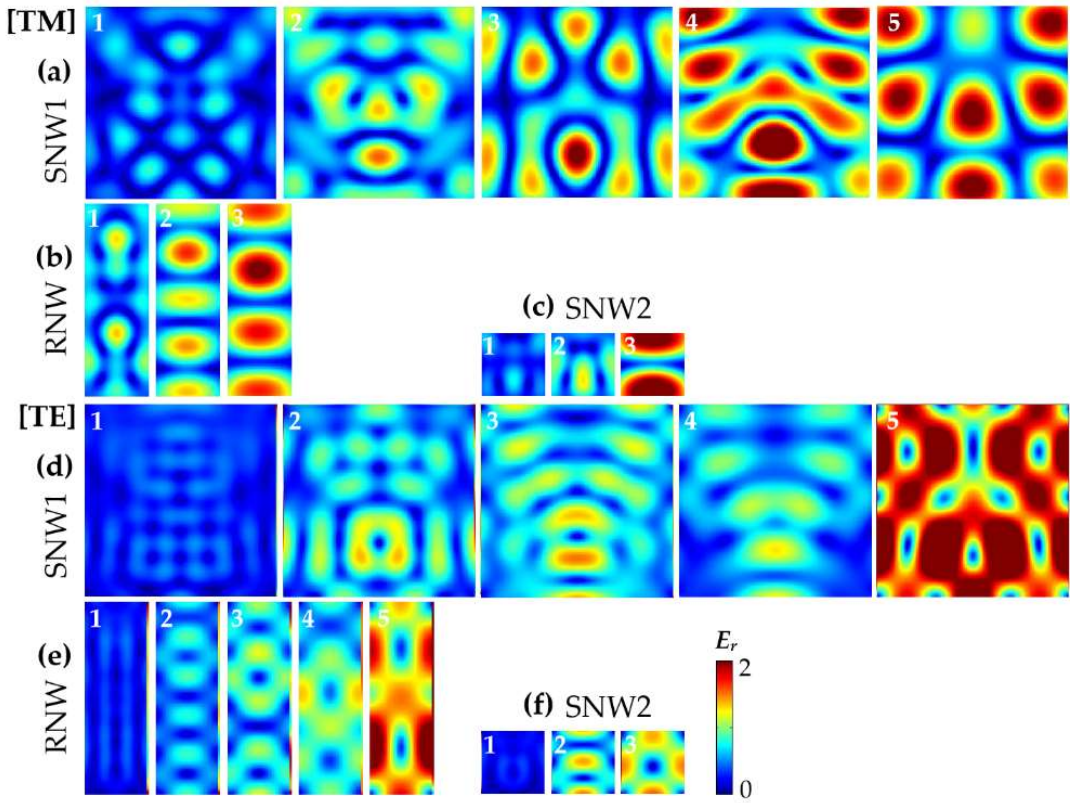

Figure 3. The representative normalized electric field (E_r) profiles of the SNW1, RNW and SNW2 at the absorption peaks indicated by numerals in Figure 2a,b: (**a**,**b**,**c**) for TM and (**d**,**e**,**f**) for TE light illumination (with an identical color scale); (**a**,**d**) for the SNW1, (**b**,**e**) for the RNW and (**c**,**f**) for the SNW2, respectively.

It is observed that there are common characteristics of the E_r profiles between the RNW and SNWs. Firstly, the improved light-harvesting of the RNW is ascribed to the excitation of the LMRs, likewise in SNW [15,16], which can confine light by multiple total internal reflections at the RNW/air interface when the wavelength of the incident light matches one of the LMRs supported by the RNW. The LMRs can be termed as TM_{ml} or TE_{ml}, where m and l describe the azimuthal mode number and the radial order of the resonances, respectively. For example, the E_r profiles of the RNW in Figure 3b(3) and Figure 3e(5) show more characteristics of the TM_{12} and TE_{31} modes of the RNW, respectively. Secondly, both NW configurations show much higher E_r intensities in the long- than in the short-wavelength range. For example, the E_r intensities for the RNW are much higher in Figure 3e(3-5) than Figure 3e(1–2) for TE light, which is attributed to the fact that ε_r'' is much smaller in the

Preprints (www.preprints.org) | NOT PEER-REVIEWED | Posted: 27 November 2020 doi:10.20944/preprints202011.0704.v1

long- than short-wavelength range, resulting in a stronger resonance. Moreover, the E_r intensities of the resonant peak in the short wavelength range are much bigger inside the whole RNW owing to the excitation of more complex LMRs (for example, Figure 3c(1) for TM light, indicating the stronger interaction of incident light with the RNW, leading to a more significant light-harvesting in comparison with the SNWs.

3.1.4. The Absorption Mode Profile (P_{abs})

To further understand the physics behind light-harvesting in single RNWs, we then examine the absorption mode profile (P_{abs}) calculated by Equation (2). In Figure 4, we present the normalized P_{abs} of the SNW1, RNW and SNW2 corresponding to the same positions denoted by numerals in Figures 2 and 3 under TM and TE light illumination, respectively. Note that Figure 4a,d show the normalized P_{abs} of the SNW1 for TM and TE light, Figure 4b,e show those of the RNW for TM and TE light, while Figure 4c,f show those of the SNW2, respectively. It is observed that the light absorption of the RNW in the short-wavelength range is much higher than that of the SNW2 (for example, Figure 3b,e(1)), leading to a significant photocurrent enhancement. Meanwhile, although the P_{abs} intensities of the RNW in the short-wavelength range is comparable with that of the SNW2, the light path length of the RNW is three times as much as that of the SNWs, resulting in a dramatic photocurrent enhancement.

It is worth noting that the match between ε_r'' and E_r becomes another essential factor in evaluating the absorption in the specific wavelength according to Equation (2). For instance, although the E_r intensities of the RNW at $\lambda = \lambda_3 = 630$ nm for TM light is much larger, the corresponding ε_r'' is the smallest, which still leads to a lower absorption, while although those of the RNW at $\lambda = \lambda_1 = 440$ nm for TM light is the smallest, the corresponding ε_r'' is much larger, which results in a more significant absorption.

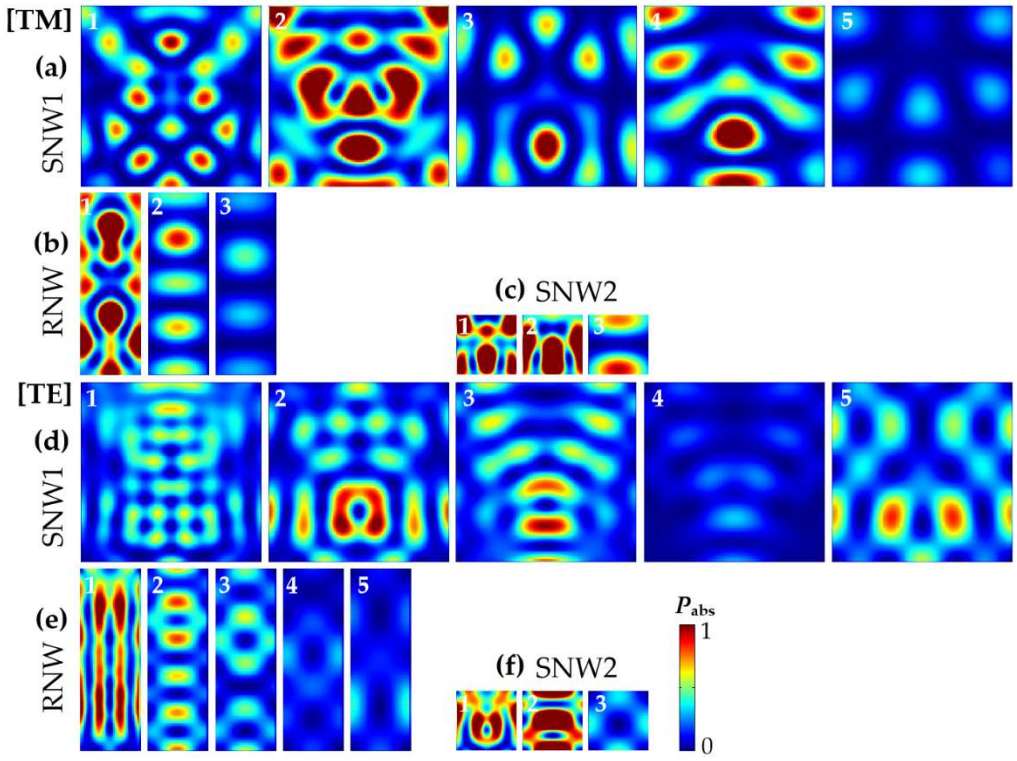

Figure 4. The representative normalized absorption mode profiles (P_{abs}) of the SNW1, RNW and SNW2 at the absorption peaks indicated by numerals in Figure 2a,b: (**a**,**b**,**c**) for TM and (**d**,**e**,**f**) for TE light illumination (with an identical color scale); (**a**,**d**) for the SNW1, (**b**,**e**) for the RNW and (**c**,**f**) for the SNW2, respectively.

Preprints (www.preprints.org) | NOT PEER-REVIEWED | Posted: 27 November 2020 doi:10.20944/preprints202011.0704.v1

3.1.5. The Photogeneration Rate (G)

To further confirm the physical mechanism discussed above, we show the photogeneration rate (G) calculated by Equation (6). In Figure 5, we present the normalized G profiles of the SNW1, RNW and SNW2 for TM and TE light illumination. Note that Figure 5a,d show the normalized G profiles of the SNW1 for TM and TE light, Figure 5b,e show those of the RNW, while Figure 5c,f show those of the SNW2, respectively. It is observed that the G intensities of the RNW are much greater in the whole NW than those of the SNW1 for both TM and TE light, and more absorption sites appear and fill in the whole RNW, leading to a giant photocurrent enhancement. Note that although the G intensities of the RNW are slightly smaller than those of the SNW2 for both TM and TE light, the light path length is three times as much as that of the SNW2, which results in a giant photocurrent enhancement. These results further demonstrate that this enhancement arises mainly from the excitation of more LMR modes caused by decreasing a compared to the SNW1 and enhanced light path length by increasing b. In other words, the RNW can better interact with the incident light compared to the SNW1 and SNW2, leading to a significant contribution to the photocurrent.

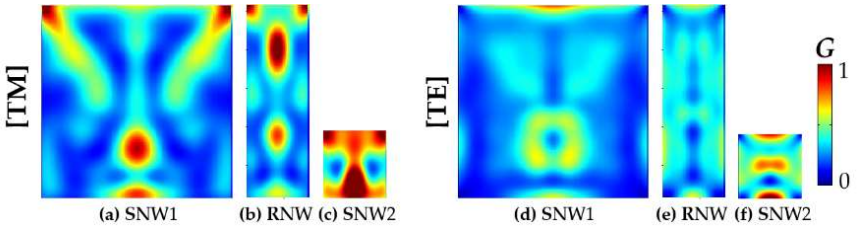

Figure 5. The normalized photogeneration rate (G) profiles for SNW1, RNW and SNW2: (a,b,c) for TM and (d,e,f) for TE light illumination (with an identical color scale); (a,d) for the SNW1, (b,e) for the RNW and (c,f) for the SNW2, respectively..

3.2. The ultimate photocurrent of Single RNWs

To verify that the improved light absorption is not just specific for the dimension discussed above, we calculate J_{ph} of the RNWs with different a (from 100 to 1000 nm) and b (from 100 to 1000 nm). In Figure 6a–c, we show 2D J_{ph} maps as a function of a and b of the RNWs for TM, TE and unpolarized light illumination, respectively. It is shown that we show J_{ph} sharply increases with decreasing a at a fixed b, reaches its maximum at a = 100 nm, and J_{ph} also dramatically increases with increasing b at a fixed a, reaches its maximum at b = 1000 nm. More importantly, J_{ph} of the RNWs is always much larger than that of the SNWs at any a (< b) values. It is observed that the maximum values of J_{ph} of the RNWs can be obtained in the length range of $100 < a < 300$ and $450 < b < 1000$ nm.

In Figure 6d,e, we show J_{ph} as a function of a of the RNWs with b = 1000 nm and J_{ph} as a function of b of the RNWs with a = 100 nm for TM, TE and unpolarized light. We then in Figure 6f,g show the photocurrent enhancement factors (PEFs) defined by Equation (9). It is observed that J_{ph} of the RNWs increases with decreasing a at a fixed b = 1000 nm and increasing b at a fixed a = 100 nm for all polarized lights, reaches 26.90, 29.50 and 28.20 mA/cm^2 at a = 100 and b = 1000 nm, which is 81.0 %, 84.6% and 82.9% much larger than that of the SNW with a = b = 1000 nm (14.86, 15.98 and 15.42 mA/cm^2) and 204.3%, 380.5% and 276.5% much larger than that of the SNW with a = b = 100 (8.84, 6.14 and 7.49 mA/cm^2) for TM, TE and unpolarized light, respectively.

Finally, we show in Figure 6h,i the normalized G profiles of two SNWs and six RNWs for TM and TE light illumination, respectively. Note here that a =1000, 500, 200 and 100 nm at fixed b = 1000 nm and b = 1000, 500, 200 and 100 nm at a fixed a = 100 nm, respectively. As shown in this figure, with the symmetry breaking from SNWs to RNWs (a = 1000 → 500 → 200 → 100 nm) with b = 1000 nm, the LMR modes are reshaped due to the size decrease of the horizontal side, and the absorption enhancement sites better fill in the whole RNWs for both TM and TE lights, especially TE light. Meanwhile, with the decreased light path length from RNWs to SNWs (b = 1000 → 500 → 200 → 100 nm) with a = 100 nm, the photocurrent is decreased.

 doi:10.20944/preprints202011.0704.v1

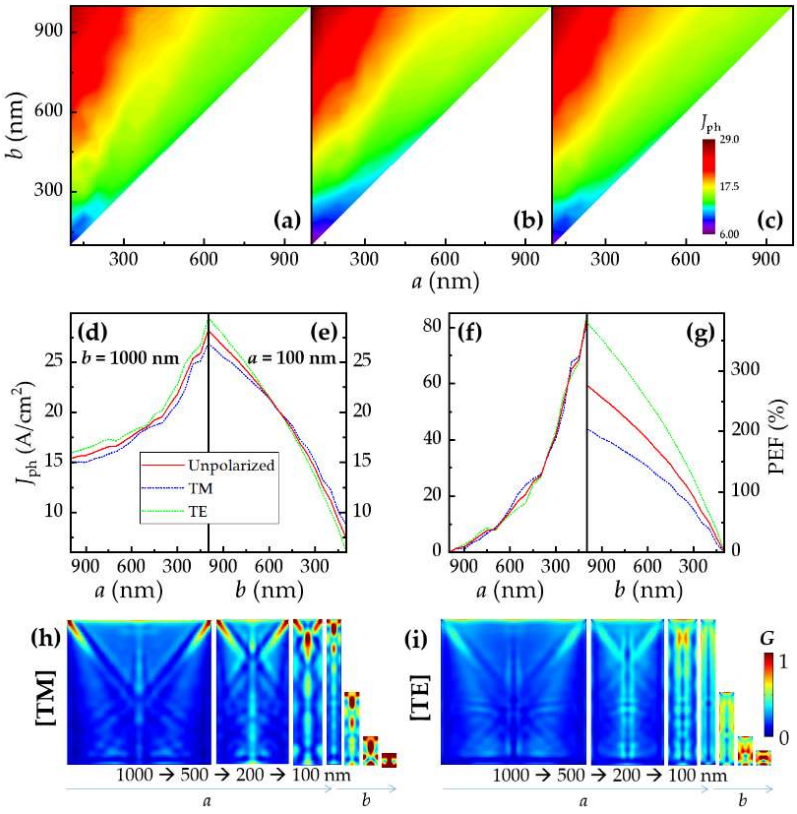

Figure 6. J_{ph} versus a and b of the RNWs for (**a**) TM, (**b**) TE and (**c**) unpolarized light illumination, respectively; (**d**) J_{ph} versus a of the RNWs with b = 1000 nm, (**e**) J_{ph} versus b of the RNWs with a = 100 nm, (**f**) The photocurrent enhancement factor (PEF) versus a of the RNWs compared to the SNW1 with the same b = 1000 nm and (**g**) PEF versus b of the RNWs compared to the SNW2 with the same a = 100 nm for TM, TE, and unpolarized light, respectively; The representative normalized G profiles of the RNWs with a = 1000, 500, 200, 100 nm at a fixed b = 1000 nm and b = 1000, 500, 200, 100 nm at a fixed a = 100 nm for (**h**) TM and (**i**) TE light illumination (with an identical color scale), respectively.

4. Conclusions

In summary, we demonstrated the effective light management from the SNWs to RNWs. The influences of the geometrical parameters of the RNWs on the light-harvesting performance were numerically investigated. It was found that the rectangular cross-section can lead to significantly improved light absorption. The examination of the spatial profiles of the electric field, absorption mode and photogeneration rate revealed that the enhancement effect resulted from the symmetry-broken structure, which can simultaneously realize the increase of the light path length by the vertical side and the reshaped LMRs by the horizontal side. The simulation results showed that the photocurrent was significantly enhanced by 276.5% or 82.9% in comparison with that of the SNW with the same side length as the horizontal side of 100 nm or the vertical side of 1000 nm, respectively. Therefore, such a RNW can be applied to various semiconductors to improve light-harvesting and provides a promising approach for the future development of high-efficiency single NW solar cells.

Author Contributions: Conceptualization, W.L.; methodology, W.L.; software, W.L.; investigation, W.L.; writing—original draft preparation, W.L.; writing—review and editing, W.L. The author have read and agreed to the published version of the manuscript.

Funding: This research was funded by the National Natural Science Foundation of China (Grant No. 61404057, 51801068 and 11875284), Key disciplines Fund for Optical Engineering in Henan Province (Grant No. 2018119) and Key Youth Teacher of Universities in Henan Province (Grant No. 2016GGJS-145).

Acknowledgments: We would like to thank the China Scholarship Council (Grant No. 201902720047) and the Master's Program on Energy and Power Engineering at Huanghuai University.

Conflicts of Interest: The authors declare no conflict of interest.

References

1. Tian, B.; Zheng, X.; Kempa, T.J.; Fang, Y.; Yu, N.; Yu, G.; Huang, J.; Lieber, C.M. Coaxial silicon nanowires as solar cells and nanoelectronic power sources. *Nature* **2007**, *449*, 885-889, doi:10.1038/nature06181.
2. Nehra, M.; Dilbaghi, N.; Marrazza, G.; Kaushik, A.; Abolhassani, R.; Mishra, Y.K.; Kim, K.H.; Kumar, S. 1D semiconductor nanowires for energy conversion, harvesting and storage applications. *Nano Energy* **2020**, *76*, 104991, doi:10.1016/j.nanoen.2020.104991.
3. Li, Z.; Tan, H.H.; Jagadish, C.; Fu, L. III–V Semiconductor Single Nanowire Solar Cells: A Review. *Adv. Mater. Technol.* **2018**, *3*, 1800005, doi:10.1002/admt.201800005.
4. Kempa, T.J.; Day, R.W.; Kim, S.-K.; Park, H.-G.; Lieber, C.M. Semiconductor nanowires: a platform for exploring limits and concepts for nano-enabled solar cells. *Energy Environ. Sci.* **2013**, *6*, 719-733, doi:10.1039/C3EE24182C.
5. Christesen, J.D.; Zhang, X.; Pinion, C.W.; Celano, T.A.; Flynn, C.J.; Cahoon, J.F. Design principles for photovoltaic devices based on Si nanowires with axial or radial p–n junctions. *Nano Lett.* **2012**, *12*, 6024-6029, doi:10.1021/nl303610m.
6. Zhan, Y.; Li, X.; Li, Y. Numerical Simulation of Light-Trapping and Photoelectric Conversion in Single Nanowire Silicon Solar Cells. *IEEE J. Sel. Top. Quantum Electron.* **2013**, *19*, 1-8, doi:10.1109/jstqe.2013.2246771.
7. Tian, B.; Kempa, T.J.; Lieber, C.M. Single nanowire photovoltaics. *Chem. Soc. Rev.* **2009**, *38*, 16-24, doi:10.1039/B718703N.
8. Tang, J.; Huo, Z.; Brittman, S.; Gao, H.; Yang, P. Solution-processed core-shell nanowires for efficient photovoltaic cells. *Nat. Nanotechnol.* **2011**, *6*, 568-572, doi:10.1038/NNANO.2011.139.
9. Heidarzadeh, H. Incident light management in a thin silicon solar cell using a two-dimensional grating according a Gaussian distribution. *Sol. Energy* **2019**, *189*, 457-463, doi:10.1016/j.solener.2019.07.099.
10. Prajapati, A.; Llobet, J.; Antunes, M.; Martins, S.; Fonseca, H.; Calaza, C.; Gaspar, J.; Shalev, G. An efficient and deterministic photon management using deep subwavelength features. *Nano Energy* **2020**, *70*, 104521, doi:10.1016/j.nanoen.2020.104521.
11. Wang, H.-P.; Lien, D.-H.; Tsai, m.-L.; Lin, C.-A.; Chang, H.-C.; Lai, K.-Y.; He, J.-H. Photon Management in Nanostructured Solar Cells. *Journal of Materials Chemistry C* **2014**, *2*, 3144-3171, doi:10.1039/C3TC32067G.
12. Narasimhan, V.K.; Cui, Y. Nanostructures for photon management in solar cells. *Nanophotonics* **2013**, 10.1515/nanoph-2013-0001, 1-24, doi:10.1515/nanoph-2013-0001.
13. Hua, B.; Lin, Q.; Zhang, Q.; Fan, Z. Efficient photon management with nanostructures for photovoltaics. *Nanoscale* **2013**, *5*, 6627-6640, doi:10.1039/c3nr01152f.
14. Chen, X.; Wang, J.; Qin, S.; Chen, Q.; Li, Y.; Li, J.; He, D. Wedge-shaped semiconductor nanowall arrays with excellent light management. *Opt. Lett.* **2017**, *42*, 3928-3931, doi:10.1364/OL.42.003928.
15. Cao, L.; White, J.S.; Park, J.-S.; Schuller, J.A.; Clemens, B.M.; Brongersma, M.L. Engineering light absorption in semiconductor nanowire devices. *Nat. Mater.* **2009**, *8*, 643-647, doi:10.1038/nmat2477.
16. Cao, L.; Fan, P.; Vasudev, A.P.; White, J.S.; Yu, Z.; Cai, W.; Schuller, J.A.; Fan, S.; Brongersma, M.L. Semiconductor Nanowire Optical Antenna Solar Absorbers. *Nano Lett.* **2010**, *10*, 439-445, doi:10.1021/nl9036627.
17. Brönstrup, G.; Jahr, N.; Leiterer, C.; Csáki, A.; Fritzsche, W.; Christiansen, S. Optical properties of individual silicon nanowires for photonic devices. *ACS Nano* **2010**, *4*, 7113-7122, doi:10.1021/nn101076t.

18. Kim, S.; Cahoon, J.F. Geometric Nanophotonics: Light Management in Single Nanowires through Morphology. *Acc. Chem. Res.* **2019**, *52*, 3511-3520, doi:10.1021/acs.accounts.9b00515.
19. Choi, J.S.; Kim, K.-H.; No, Y.-S. Spatially localized wavelength-selective absorption in morphology-modulated semiconductor nanowires. *Opt. Express* **2017**, *25*, 22750-22759, doi:10.1364/OE.25.022750.
20. Zhang, C.; Yang, Z.; Wu, K.; Li, X. Design of asymmetric nanovoid resonator for silicon-based single-nanowire solar absorbers. *Nano Energy* **2016**, *27*, 611-618, doi:10.1016/j.nanoen.2016.08.017.
21. Luo, S.; Yu, W.B.; He, Y.; Ouyang, G. Size-dependent optical absorption modulation of Si/Ge and Ge/Si core/shell nanowires with different cross-sectional geometries. *Nanotechnology* **2015**, *26*, 085702, doi:10.1088/0957-4484/26/8/085702.
22. Kim, S.-K.; Song, K.-D.; Kempa, T.J.; Day, R.W.; Lieber, C.M.; Park, H.-G. Design of Nanowire Optical Cavities as Efficient Photon Absorbers. *ACS Nano* **2014**, *8*, 3707–3714, doi:10.1021/nn5003776.
23. Kim, S.-K.; Day, R.W.; Cahoon, J.F.; Kempa, T.J.; Song, K.-D.; Park, H.-G.; Lieber, C.M. Tuning Light Absorption in Core/Shell Silicon Nanowire Photovoltaic Devices through Morphological Design. *Nano Lett.* **2012**, *12*, 4971-4976, doi:10.1021/nl302578z.
24. Kempa, T.J.; Cahoon, J.F.; Kim, S.-K.; Day, R.W.; Bell, D.C.; Park, H.-G.; Lieber, C.M. Coaxial multishell nanowires with high-quality electronic interfaces and tunable optical cavities for ultrathin photovoltaics. *P. Natl. Acad. Sci. USA* **2012**, *109*, 1407-1412, doi:10.1073/pnas.1120415109.
25. Liu, W.; Oh, J.I.; Shen, W.Z. Light Trapping in Single Coaxial Nanowires for Photovoltaic Applications. *IEEE Electron Device Lett.* **2011**, *32*, 45-47, doi:10.1109/LED.2010.2086428.
26. Liu, W.; Oh, J.I.; Shen, W.Z. Light absorption mechanism in single c-Si (core)/a-Si (shell) coaxial nanowires. *Nanotechnology* **2011**, *22*, 125705, doi:10.1088/0957-4484/22/12/125705.
27. Liu, W.; Guo, X.; Xing, S.; Yao, H.; Wang, Y.; Bai, L.; Wang, Q.; Zhang, L.; Wu, D.; Zhang, Y., et al. Off-Resonant Absorption Enhancement in Single Nanowires via Graded Dual-Shell Design. *Nanomaterials* **2020**, *10*, 1740, doi:10.3390/nano10091740.
28. Zhong, Z.; Li, Z.; Gao, Q.; Li, Z.; Peng, K.; Li, L.; Mokkapati, S.; Vora, K.; Wu, J.; Zhang, G., et al. Efficiency enhancement of axial junction InP single nanowire solar cells by dielectric coating. *Nano Energy* **2016**, *28*, 106-114, doi:10.1016/j.nanoen.2016.08.032.
29. Solanki, A.; Gentile, P.; Boutami, S.; Calvo, V.; Pauc, N. Dielectric Coating-Induced Absorption Enhancement in Si Nanowire Junctions. *Adv. Opt. Mater.* **2015**, *3*, 120-128, doi:10.1002/adom.201400334.
30. Kim, S.-K.; Zhang, X.; Hill, D.J.; Song, K.-D.; Park, J.-S.; Park, H.-G.; Cahoon, J.F. Doubling Absorption in Nanowire Solar Cells with Dielectric Shell Optical Antennas. *Nano Lett.* **2015**, *15*, 753-758, doi:10.1021/nl504462e.
31. Yu, Y.; Ferry, V.E.; Alivisatos, A.P.; Cao, L. Dielectric Core–Shell Optical Antennas for Strong Solar Absorption Enhancement. *Nano Lett.* **2012**, *12*, 3674-3681, doi:10.1021/nl301435.
32. Li, X.; Zhan, Y.; Wang, C. Broadband enhancement of coaxial heterogeneous gallium arsenide single-nanowire solar cells. *Prog. Photovolt. Res. Appl.* **2015**, *23*, 628-636, doi:10.1002/pip.2480.
33. Yang, Z.; Cao, G.; Shang, A.; Lei, D.Y.; Zhang, C.; Gao, P.; Ye, J.; Li, X. Enhanced Photoelectrical Response of Hydrogenated Amorphous Silicon Single-Nanowire Solar Cells by Front-Opening Crescent Design. *Nanoscale Res. Lett.* **2016**, *11*, 233, doi:10.1186/s11671-016-1447-0.
34. Yang, Z.; Li, X.; Lei, D.Y.; Shang, A.; Wu, S. Omnidirectional absorption enhancement of symmetry-broken crescent-deformed single-nanowire photovoltaic cells. *Nano Energy* **2015**, *13*, 9-17, doi:10.1016/j.nanoen.2015.02.007.

35. Zhang, C.; Yang, Z.; Shang, A.; Wu, S.; Zhan, Y.; Li, X. Improved optical absorption of silicon single-nanowire solar cells by off-axial core/shell design. *Nano Energy* **2015**, *17*, 233-240, doi:10.1016/j.nanoen.2015.08.017.
36. Shi, L.; Zhou, Z.; Huang, Z. The influence of silver core position on enhanced photon absorption of single nanowire a-Si solar cells. *Opt. Express* **2013**, *21*, A1007-A1017, doi:10.1364/oe.21.0a1007.
37. Zhou, J.; Zhang, Z.; Wu, Y.; Xia, Z.; Qin, X. Significantly enhanced coupling to half-space irradiation using a partially capped nanowire for solar cells. *Nano Energy* **2018**, *45*, 61-67, doi:10.1016/j.nanoen.2017.12.027.
38. Leahu, G.; Petronijevic, E.; Belardini, A.; Centini, M.; Sibilia, C.; Hakkarainen, T.; Koivusalo, E.; Rizzo Piton, M.; Suomalainen, S.; Guina, M. Evidence of Optical Circular Dichroism in GaAs-Based Nanowires Partially Covered with Gold. *Adv. Opt. Mater.* **2017**, *5*, 1601063, doi:10.1002/adom.201601063.
39. Mann, S.A.; Garnett, E.C. Extreme Light Absorption in Thin Semiconductor Films Wrapped around Metal Nanowires. *Nano Lett.* **2013**, *13*, 3173-3178, doi:10.1021/nl401179h.
40. Jia, Y.; Qiu, M.; Wu, H.; Cui, Y.; Fan, S.; Ruan, Z. Theory of Half-space Light Absorption Enhancement for Leaky Mode Resonant Nanowires. *Nano Lett.* **2015**, *15*, 5513-5518, doi:10.1021/acs.nanolett.5b02044.
41. Wang, B.; Leu, P.W. Enhanced absorption in silicon nanocone arrays for photovoltaics. *Nanotechnology* **2012**, *23*, 194003, doi:10.1088/0957-4484/23/19/194003.
42. Wang, B.; Stevens, E.; Leu, P.W. Strong broadband absorption in GaAs nanocone and nanowire arrays for solar cells. *Opt. Express* **2014**, *22*, A386-A395, doi:10.1364/OE.22.00A386.
43. Anttu, N.; Mäntynen, H.; Sorokina, A.; Kivisaari, P.; Sadi, T.; Lipsanen, H. Geometry Tailoring of Emission from Semiconductor Nanowires and Nanocones. *Photonics* **2020**, *7*, 23, doi:10.3390/photonics7020023.
44. Zhou, L.; Yu, X.; Zhu, J. Metal-Core/Semiconductor-Shell Nanocones for Broadband Solar Absorption Enhancement. *Nano Lett.* **2014**, *14*, 1093-1098, doi:10.1021/nl500008y.
45. Xu, Z.; Huangfu, H.; He, L.; Wang, J.; Yang, D.; Guo, J.; Wang, H. Light-trapping properties of the Si inclined nanowire arrays. *Opt. Commun.* **2017**, *382*, 332-336, doi:10.1016/j.optcom.2016.08.018.
46. Kayes, M.; Leu, P. Comparative study of absorption in tilted silicon nanowire arrays for photovoltaics. *Nanoscale Res. Lett.* **2014**, *9*, 620, doi:10.1186/1556-276X-9-620.
47. Hong, L.; Rusli; Wang, X.; Zheng, H.; Wang, H.; Yu, H. Design guidelines for slanting silicon nanowire arrays for solar cell application. *J. Appl. Phys.* **2013**, *114*, 084303-084306, doi:10.1063/1.4819175.
48. Adibzadeh, F.; Olyaee, S. Optical absorption enhancement in vertical InP nanowire random structures for photovoltaic applications. *Opt. Quantum Electron.* **2020**, *52*, 6, doi:10.1007/s11082-019-2120-5.
49. Qin, X.; Wu, Y.; Zhang, Z.; Xia, Z.; Zhou, J.; Zhu, J. Broadband light absorption enhancement in randomly rotated elliptical nanohole arrays for photovoltaic application. *Appl. Opt.* **2019**, *58*, 1152-1157, doi:10.1364/AO.58.001152.
50. Zhang, H.; Kramarenko, M.; Osmond, J.; Toudert, J.; Martorell, J. Natural Random Nanotexturing of the Au Interface for Light Backscattering Enhanced Performance in Perovskite Solar Cells. *ACS Photonics* **2018**, 10.1021/acsphotonics.8b00099, doi:10.1021/acsphotonics.8b00099.
51. Dhindsa, N.; Saini, S.S. Comparison of ordered and disordered silicon nanowire arrays: experimental evidence of photonic crystal modes. *Opt. Lett.* **2016**, *41*, 2045-2048, doi:10.1364/OL.41.002045.
52. Bao, H.; Ruan, X. Optical absorption enhancement in disordered vertical silicon nanowire arrays for photovoltaic applications. *Opt. Lett.* **2010**, *35*, 3378-3380, doi:10.1364/OL.35.003378.
53. Khaled, A.; Hameed, M.F.O.; Rahman, B.M.A.; Grattan, K.T.V.; Obayya, S.S.A.; Hussein, M. Characteristics of silicon nanowire solar cells with a crescent nanohole. *Opt. Express* **2020**, *28*, 31020-31033, doi:10.1364/OE.397051.

54. Liu, W.; Wang, Y.; Guo, X.; Song, J.; Wang, X.; Yi, Y. Light Trapping in Single Elliptical Silicon Nanowires. *Nanomaterials* **2020**, *10*, 12121, doi:10.3390/nano10112121.
55. Li, X.; Zhan, Y. Enhanced external quantum efficiency in rectangular single nanowire solar cells. *Appl. Phys. Lett.* **2013**, *102*, 021101, doi:10.1063/1.4775578.
56. Wangyang, P.; Wang, Q.; Wan, X.; Hu, K.; Huang, K. Optical absorption enhancement in silicon square nanohole and hybrid square nanowire-hole arrays for photovoltaic applications. *Opt. Commun.* **2013**, *294*, 377–383, doi:10.1016/j.optcom.2012.12.040.
57. Deng, W.; Peng, X.; Zou, J.; Wang, W.; Liu, Y.; Zhang, T.; Zhang, Y.; Zhang, D. Comparison of photoemission characteristics between square and circular wire array GaAs photocathodes. *Appl. Opt.* **2017**, *56*, 8991-8995, doi:10.1364/AO.56.008991.
58. Palik, E.D. *Handbook of Optical Constants of Solids*; Academic Press: London, UK, 1985.
59. Kane, Y. Numerical Solution of Initial Boundary Value Problems Involving Maxwell's Equations in Isotropic Media. *IEEE Trans. Antennas Propag.* **1966**, *14*, 302-307, doi:10.1109/TAP.1966.1138693.
60. Taflove, A.; Hagness, S.C. *Computational Electrodynamics: The Finite-Difference Time-Domain Method*, 3rd ed.; Artech House: Norwood, MA, USA, 2005.
61. Ee, H.S.; Song, K.D.; Kim, S.K.; Park, H.G. Finite-Difference Time-Domain Algorithm for Quantifying Light Absorption in Silicon Nanowires. *Isr. J. Chem.* **2012**, *52*, 1027-1036, doi:10.1002/ijch.201200061.
62. Bohren, C.F.; Huffman, D.R. *Absorption and Scattering of Light by Small Particles* John Wiley & Sons, Inc.: New York, USA, 1998.
63. Ferry, V.E.; Polman, A.; Atwater, H.A. Modeling light trapping in nanostructured solar cells. *ACS Nano* **2011**, *5*, 10055-10064, doi:10.1021/nn203906t.
64. Munday, J.N.; Atwater, H.A. Large integrated absorption enhancement in plasmonic solar cells by combining metallic gratings and antireflection coatings. *Nano Lett.* **2010**, *11*, 2195-2201, doi:10.1021/nl101875t.